Long-range wall perturbations in dense granular flows

Pierre G. Rognon[1,2,†], **Thomas Miller**[1,3], **Bloen Metzger**[2] **and Itai Einav**[1]

[1]Particles and Grains Laboratory, School of Civil Engineering, The University of Sydney, Sydney, NSW 2006, Australia

[2]IUSTI-CNRS UMR 7343, Aix-Marseille University, 13453 Marseille, France

[3]Department of Civil, Environmental and Geomatic Engineering, Faculty of Engineering Science, University College London, Gower Street, London WC1E 6BT, UK

We explore how the rheology of dense granular flows is affected by the presence of sidewalls. The study is based on discrete element method simulations of plane-shear flows between two rough walls, prescribing both the normal stress and the shear rate. Results confirm previous observations for different systems: large layers near the walls develop where the local viscosity is not constant, but decreases when approaching the walls. The size of these layers can reach several dozen grain diameters, and is found to increase when the flow decelerates, as a power law of the inertial number. Two non-local models are found to adequately explain such features, namely the kinetic elasto-plastic fluidity (KEP) model and the eddy viscosity model (EV). The analysis of the internal kinematics further shows that the vorticity and its associated length scale may be a key component of these non-local behaviours.

Key words: granular mixing, particle/fluid flow, rheology

1. Introduction

When subjected to sufficient stresses, dense granular materials flow. This property is at the core of various industrial processes involving manufacturing and transport of various kinds of powders and grains. It is also at the core of the dynamics of geophysical flows such as landslides and snow avalanches. A robust and accurate modelling of the flowing behaviour of dense granular materials is needed for these applications.

Dense granular flows exhibit a non-Newtonian behaviour. They are characterised by a visco-plastic constitutive law, that relates the local stresses to the local strain rates (GDR MiDi 2004; da Cruz *et al.* 2005; Jop, Forterre & Pouliquen 2006; Andreotti 2007; Forterre & Pouliquen 2008; Andreotti, Forterre & Pouliquen 2013). This constitutive law is sufficient to describe dense granular flows far from walls in various geometries. However, it generally fails to predict the flow close to walls.

The presence of walls in granular flows may induce two important effects. First, with smooth walls some slip velocity may develop. This slip velocity vanishes for

† Email address for correspondence: pierre.rognon@sydney.edu.au

rough walls featuring asperities larger than the grain size (Goujon, Thomas & Dalloz-Dubrujeaud 2003; Shojaaee *et al.* 2012*a*,*b*). Second, even without slip velocity, the behaviour of the flowing granular materials appears to be strongly modified near walls. Such effects were interpreted as resulting from the non-local behaviour of granular materials: the ability to flow at a given location depends on the nature of the flow in the surrounding region.

Various models have been developed and have successfully captured such non-local effects. They are based on Cosserat-plasticity (Mohan, Rao & Nott 2002), visco-plasticity combined with non-local self-activated processes (NL model) (Pouliquen & Forterre 2001, 2009) or non-local kinetic elasto-plastic fluidity (KEP model) (Goyon *et al.* 2008; Kamrin & Koval 2012; Bouzid *et al.* 2013; Mansard *et al.* 2013). These models involve some typical length characterising the extent of the non-locality. This length was found to increase as the flows decelerate and stop. These models successfully capture and rationalise non-trivial variations in local viscosities and jamming conditions within flows featuring stresses and shear rate gradients, such as cylindrical-Couette flows, plane-shear flows with or without gravity, flows down a slope and flows in pipes. However, the predictions of these models critically rely on the assumptions made regarding the role of bounding walls. With the NL model, walls may be assumed either to absorb stress fluctuations coming from the flowing materials or to reflect them back into the flow. Depending on which of these two assumptions is considered, the model predicts an increase or a decrease in local viscosity near walls. Similarly, the variation in viscosity near walls predicted by the KEP model strongly depends on the value of the material's fluidity at the wall, which needs to be assumed or empirically determined for each flow configuration.

Another type of non-local model, inspired by the eddy viscosity (EV model) concept developed in turbulence, was introduced to predict the variation in viscosity near walls without relying on such assumptions. This model successfully captured the variation in granular viscosity near walls measured numerically in flow down a slope (Staron 2008; Staron *et al.* 2010), and experimentally in plane-shear flows (Miller *et al.* 2013; Miller 2014). Nonetheless, the validity of the model was only demonstrated for narrow systems in quasi-static flow regimes, and whether or not it could capture similar non-local features in larger systems and faster flows is still an open question. Further, this model is based on the existence of large granular vortices, whose typical size would decrease near walls. However, the existence of such a vorticity length scale has not been demonstrated, and there is no consensus on how it should evolve near walls.

In this paper, we investigate the range and the nature of wall perturbations in dense granular flows. To this end, we use a discrete element method to simulate the flow of a two-dimensional granular material between two parallel walls, prescribing both the shear rate and the normal stress. We analyse the stresses and strain rate near the walls to demonstrate possible deviations from the constitutive law predictions. The goal is to establish an empirical model describing these deviations, and discuss how they can be rationalised by non-local models.

The simulated system will be presented in § 2. In § 3 we present the measurements of the macroscopic friction and dilatancy laws as a function of the system size. In § 4, we analyse the stresses and strain rates within the flows to demonstrate long-range wall perturbations, and propose an empirical model capturing their observed features. In § 5, we discuss how such wall effects can be captured by the KEP and EV non-local models, and we analyse the internal flow kinematics to support the relevance of these models, focusing on the local vorticity and its associated length scale.
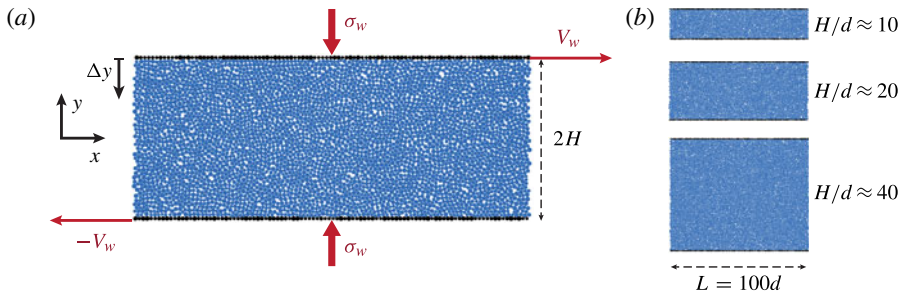
FIGURE 1. (Colour online) Plane-shear flow geometry. (*a*) Thousands of grains are subjected to shear between two rough walls (black grains) imposing both shear rate $\dot{\Gamma}_w = V_w/H$ and normal stress σ_M. Periodic boundaries are applied in the *x*-direction. (*b*) Three systems with different half-widths H are analysed.

2. Dense granular flows in the plane-shear geometry

In this section, we present the simulated system and define the measured quantities.

2.1. *Plane-shear geometry*

We consider flows in a plane-shear geometry as illustrated in figure 1(*a*). It comprises two parallel walls shearing a two-dimensional assembly of grains, prescribing both shear rate and normal stress. The wall separation distance is $2H$. They are made out of aligned grains having the same mechanical and physical properties as the flowing grains. The wall velocity in the shear direction *x*, V_w, is controlled such that the macroscopic shear rate,

$$\dot{\Gamma}_M = \frac{V_w}{H}, \tag{2.1}$$

is constant in time. The wall separation distance, $2H(t)$, is free to vary in time in order to ensure that the external stress, σ_w, is balanced by the total force of the grains contacting the wall, F^{int}. $H(t)$ satisfies inertial dynamics, $M\ddot{H} = F^{int} - \sigma_w L d$, with M being the total mass of the walls.

2.2. *Grain properties*

The grains are disks of density ρ, mass m and diameter d. A polydispersity of $\pm 20\,\%$ is introduced in the grain diameter to avoid crystallisation. Grains interact with their neighbours through inelastic and frictional contacts. These interaction laws are detailed in appendix A. They only depend on the elastic coefficient of the grains, E (Pa), Newton's coefficient of restitution, e, and the coefficient of friction between two grains, μ_g. Unless otherwise specified, the grain-to-grain friction and restitution coefficient are set to $\mu_g = 0.5$ and $e = 0.5$, respectively. The value of the deformation number, $\kappa = \sigma_w/E = 10^{-3}$, is fixed to be in the rigid-grain limit, characterised by small elastic deformations (see appendix A).

2.3. *Numerical experiments*

The numerical experiments comprise two steps: the preparation of a steady flow, and the steady flow during which measurements are performed. The preparation of the

steady flow consists of applying both normal stress, σ_w, and shear rate, $\dot{\Gamma}_M$, on a loose configuration of grains, initially set randomly with no contact. The system width, $H(t)$, decreases and the solid fraction ϕ_M, the ratio of the grain surface area to the total system area, increases. They both eventually reach steady-state values with small time fluctuations.

In the following, the analysis will focus on steady flows in systems of varying width, $H/d = 10$, 20, and 40 (see figure 1b), with different values of the macroscopic inertial number I_M,

$$I_M = \dot{\Gamma}_M d \sqrt{\frac{\rho}{\sigma_w}}, \qquad (2.2)$$

ranging from 10^{-3} to 10^{-1}, which corresponds to flows in the dense regime (GDR MiDi 2004; da Cruz *et al.* 2005).

2.4. *Macroscopic quantities and profiles*

In the following, the analysis will be based on quantities such as stresses, velocities, velocity gradient and solid fraction in the steady regime. These quantities will be averaged in time by considering a set of 100 snapshots, the system undergoing a shear deformation of one between two consecutive snapshots. We will distinguish the macroscopic quantities corresponding to a spatial average over the entire system, denoted by a subscript M, from their profile along the transverse direction y, obtained by averaging in the direction of shear, x, and in time, using the procedure described in appendix B.

We denote as ϕ_M, τ_M, σ_M and $\dot{\Gamma}_M$ the macroscopic solid fraction, shear and normal stresses and shear rate; $\phi(y)$, $\tau(y)$, $\sigma(y)$ and $\dot{\gamma}(y)$ refers to their profiles. The relationship between macroscopic quantities and their profile is, taking the example of the solid fraction, $\phi_M = (1/2H) \int_{-H}^{H} \phi(y) \mathrm{d}y$.

3. Effect of system size on macroscopic friction and dilatancy laws

As a way to demonstrate possible wall effects in our systems, let us first analyse the stresses and strain rate at a macroscopic level in our systems by comparing them with the prediction of the visco-plastic constitutive law of dense granular flows.

3.1. *Local friction and dilatancy laws*

The local visco-plastic constitutive law describing dense granular flow can be expressed by a friction law combined with a dilatancy law (GDR MiDi 2004; da Cruz *et al.* 2005; Jop *et al.* 2006; Forterre & Pouliquen 2008; Andreotti *et al.* 2013). These two laws specify how the effective friction coefficient, μ, the ratio of the shear and normal stresses, and the solid fraction, ϕ, depend on the shear rate $\dot{\gamma}$. In the dense regime, both laws are approximately linear functions of the local shear rate:

$$\mu(y) = \frac{\tau(y)}{\sigma(y)} \approx \mu_s + aI(y), \qquad (3.1)$$

$$\phi(y) \approx \phi_0 - bI(y), \qquad (3.2)$$

$$I(y) = \dot{\gamma}(y) d \sqrt{\frac{\rho}{\sigma(y)}}. \qquad (3.3)$$

The coefficients μ_s, a, ϕ_0 and b are positive numerical constants which depend on the nature of the grains and of their interactions, such as friction, shape and adhesion (da Cruz *et al.* 2005; Rognon *et al.* 2006, 2007, 2008).
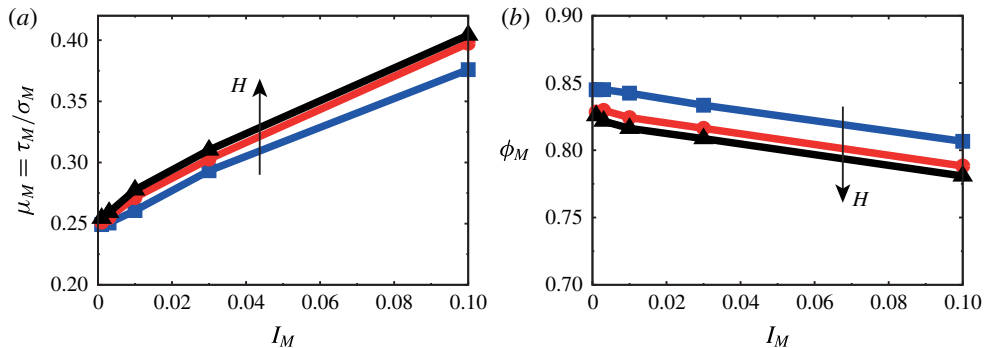
FIGURE 2. (Colour online) Macroscopic constitutive behaviour measured in systems of differing sizes $H/d = 10$ (■), 20 (●) and 40 (▲): (*a*) friction law and (*b*) dilatancy law.

3.2. *Macroscopic friction and dilatancy laws*

In steady sheared flows between two parallel plates, the momentum balance predicts that there should be no stress gradient in the transverse direction y, $\sigma(y) = \sigma_w = \sigma_M$ and $\tau(y) = \tau_M$. According to (3.1) and (3.2), the local shear rate and solid fraction should thus be constant: $\dot{\gamma}(y) = \dot{\Gamma}_M$ and $\phi(y) = \phi_M$. Integrating the local friction and dilatancy laws would thus lead to a macroscopic expression for the constitutive behaviour of the form

$$\mu_M = \frac{\tau_M}{\sigma_M} \approx \mu_s + aI_M, \tag{3.4}$$

$$\phi_M \approx \phi_0 - bI_M. \tag{3.5}$$

We measured such macroscopic laws in our systems (see figure 2). For a given system width H, the macroscopic friction and dilatancy laws approximately exhibit a linear dependence on the macroscopic inertial number I_M (2.2), consistent with (3.4) and (3.5). However, with the same inertial number I_M different values of the macroscopic coefficient of friction and solid fraction are obtained in systems of differing width H. Larger systems leads to higher coefficient of friction μ_M and lower solid fraction ϕ_M.

The local visco-plastic constitutive law as expressed in (3.4) and (3.5) does not predict this system size effect. It suggests that walls may affect the material rheology, and the next sections will focus on characterising and understanding such an effect.

4. Characterisation of long-range wall perturbations

In this section we analyse the profiles of stresses, solid fraction and shear rate to characterise the effect of walls in the flowing behaviour of the materials.

4.1. *Demonstrating wall effects*

Let us first describe a particular flow obtained with $I_M = 10^{-2}$ and $H/d = 20$. We observe that the local friction coefficient, $\mu(y) = \tau(y)/\sigma(y)$, is constant (see figure 3a). This is consistent with the momentum balance applied to this geometry, which predicts no stress gradient in the y-direction. The solid fraction $\phi(y)$ is also mostly constant, but slightly decreases in the wall vicinity. The important result is that, although
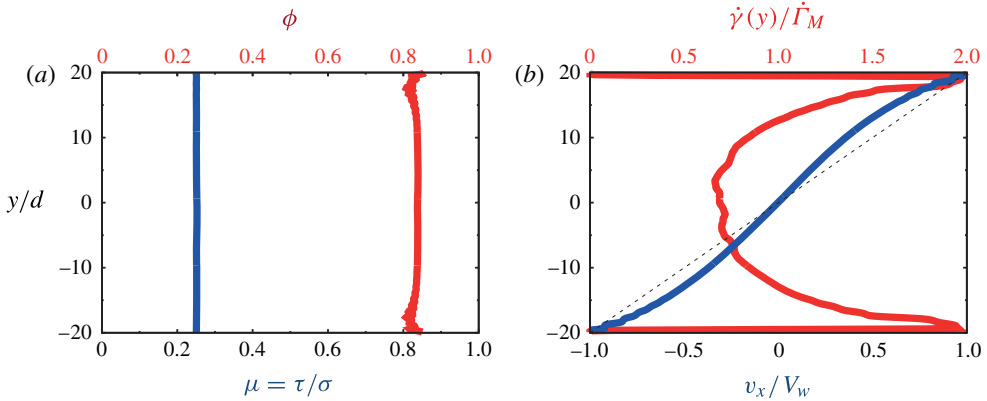
FIGURE 3. (Colour online) Time-averaged profiles along the y-direction within a steady flow ($H = 20d$, $I_M = 0.01$). (*a*) Friction coefficient, ratio of shear to normal stresses $\mu(y) = \tau(y)/\sigma(y)$ (bottom axis, dark grey curve, blue online) and solid fraction $\phi(y)$ (top axis, light grey curve, red online). (*b*) Velocity profile $v_x(y)$ normalised by the wall velocity V_w (bottom axis, dark grey curve, blue online) and the linear velocity profile $V_w y/H$ is shown for comparison (dashed line); and shear rate $\dot{\gamma}(y)$ normalised by the nominal shear rate $\dot{\Gamma}_M = V_w/H$ (top axis, light grey curve, red online).

stresses are constant throughout the layer, the velocity profile $v_x(y)$ is not linear (see figure 3*b*) but exhibits an S-shape. The corresponding shear rate profile,

$$\dot{\gamma}(y) = \frac{\partial v_x(y)}{\partial y}, \qquad (4.1)$$

is thus not constant. It increases significantly when approaching the walls while staying approximately constant in the central region of the flow. Similar S-shape profiles in plane-shear flows were reported in da Cruz *et al.* (2004), GDR MiDi (2004), Miller *et al.* (2013) and Miller (2014).

The fact that the shear rate $\dot{\gamma}(y)$ varies near the wall while the stresses are constant shows that the local friction and dilatancy laws in (3.1) and (3.2) fail to describe the flow in these regions. An additional effect of the walls leads to an increase of the local shear rate in the wall vicinity.

Flows were computed varying two grain contact parameters: their coefficient of friction μ_g and the coefficient of restitution e. Figure 4 shows that similar non-constant shear rate profiles are obtained when varying these parameters, even with frictionless grains ($\mu_g = 0$). This suggests that neither the friction nor restitution coefficient is responsible for the curvature of the velocity profile.

4.2. *Shear rate variation near walls*

Figure 5(*a*) shows the variation in shear rate as a function of the distance to the wall Δy:

$$\Delta y = H - |y|, \qquad (4.2)$$

for $H = 40d$ and $I_M = 10^{-2}$. The shear rate is maximum near the wall and approximately constant in a first layer of size $\delta \approx 2d$. For $\Delta y > \delta$, the shear rate
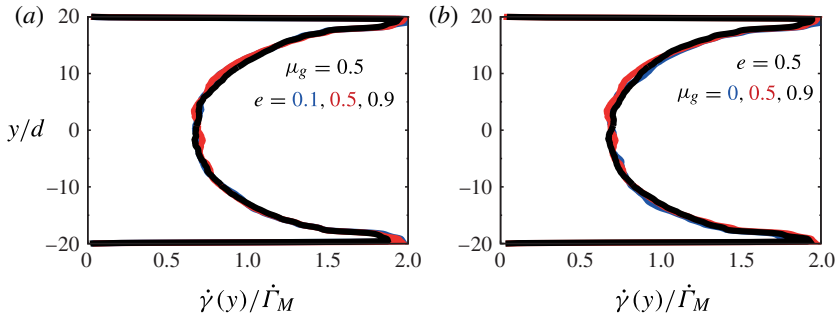
FIGURE 4. (Colour online) Shear rate profiles along the y-direction within steady flows ($H = 20d$, $I_w = 0.01$) for (*a*) differing contact restitution coefficient e (0.1, dark grey, blue online; 0.5, light grey, red online; 0.9, black) and (*b*) differing contact friction coefficient μ_g (0, dark grey, blue online; 0.5, light grey, red online; 0.9, black).
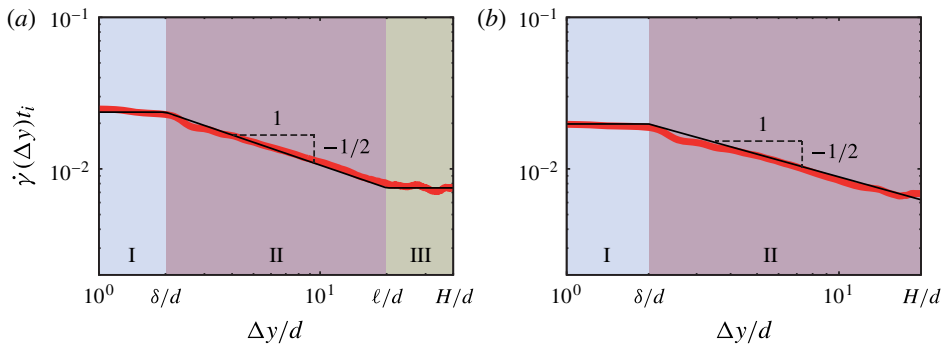

FIGURE 5. (Colour online) Shear rate $\dot{\gamma}$ versus distance to the wall Δy for two simulations with similar inertial number, $I_M = 10^{-2}$, but different widths: (*a*) $H/d = 40$ and (*b*) $H/d = 20$. The wall is at $\Delta y = 0$ while the centre of the sheared layer is at $\Delta y = H$. The shear rate, $\dot{\gamma}$, is expressed in inverse unit of inertial time, $t_i = d\sqrt{\rho_g/\sigma_M}$. Thick grey lines (red online) represent simulation results and thin black lines the empirical model defined in (4.4).

decreases when the distance to the wall Δy increases. In this zone, the shear rate decay can be represented by a power law:

$$\dot{\gamma}(y) \propto (\Delta y)^{-1/2}. \tag{4.3}$$

For large distance to the wall, $\Delta y > \ell$, the shear rate seems again constant.

Figure 5(*b*) shows the shear rate profile $\dot{\gamma}(\Delta y)$ for a flow with the same inertial number as in figure 5(*a*), but in a narrower system, $H = 20d$. The first layer of constant shear rate for $\Delta y < \delta \approx 2d$ and the second layer of decaying shear rate for $\Delta y > \delta \approx 2d$ are still present. However, in this case the shear rate decays until the middle of the flow and there is thus no central zone with a constant shear rate.

4.3. *Empirical model capturing shear rate profiles*

The profiles shown on figure 5 suggest how the shear rate can be modelled in each of the three zones, I, II and III. Accounting for the fact that the shear rate is continuous,

these profiles can be captured by the following empirical model:

$$\dot{\gamma}(\Delta y) = \begin{cases} \dot{\gamma}_b \sqrt{\dfrac{\ell}{\delta}} : \Delta y \leqslant \delta & \text{(I)} \\[2ex] \dot{\gamma}_b \sqrt{\dfrac{\ell}{\Delta y}} : \delta \leqslant \Delta y \leqslant \ell & \text{(II)} \\[2ex] \dot{\gamma}_b : \ell \leqslant \Delta y \leqslant H & \text{(III).} \end{cases} \tag{4.4}$$

The numerical results shown in figures 5(*a*) and 5(*b*) are both captured by this empirical model using $\delta = 2d$, $\ell = 20d$ and $\dot{\gamma}_b = 0.75\,\dot{\Gamma}_M$, where $\dot{\gamma}_b$ is the bulk shear rate.

4.4. *Range of wall perturbations*

We denote as ℓ the range of the wall perturbations, the region comprising zones I and II ($0 < \Delta y < \ell$) where the shear rate differs from the constant bulk value found in zone III.

For the flow conditions of figure 5(*a*), the wall perturbation range is remarkably large, $\ell \approx 20d$. Within the same conditions, $I_M = 10^{-2}$, but in a narrower system, $H = 20d$, zone III no longer exists (see figure 5*b*) which can be interpreted as an overlap of the perturbations from each wall.

Figure 6 shows the velocity and shear rate profiles for flows with various inertial numbers I_M and various widths H. For large systems, the wall perturbation range seems to increase as the inertial number decreases, and never exceeds the system width. For narrow systems, the wall perturbation spans the entire system width.

In the largest system, $H = 40d$, the size ℓ of the wall perturbation is estimated for flows of different internal number I_M by adjusting the empirical model (4.4) to the measured shear rate profiles. Figure 7(*a*) shows the best fit of the empirical model to the measured shear rate profiles. All the shear rate profiles were captured by the model using similar values of δ ranging between 1.5 and 2. Conversely, the range of the wall perturbation, ℓ, was found to vary from $6.5d$ to $25d$.

Figure 7(*b*) shows the values of wall perturbation range ℓ thus estimated as a function of the macroscopic inertial number I_M. For macroscopic inertial number ranging from 6×10^{-3} to 10^{-1}, the size of the wall perturbation exhibits a power law:

$$\frac{\ell}{d} \approx 2I_M^{-1/2}. \tag{4.5}$$

For the lowest inertial numbers, ℓ could not be estimated since zone III did not exist even in the largest systems.

5. Modelling wall perturbations

In the previous section, we have identified two empirical laws: one capturing the increase in shear rate observed near walls (4.4) and the other capturing the range of this perturbation (4.5). Let us now discuss the mechanisms and analytical models that may explain these perturbations.
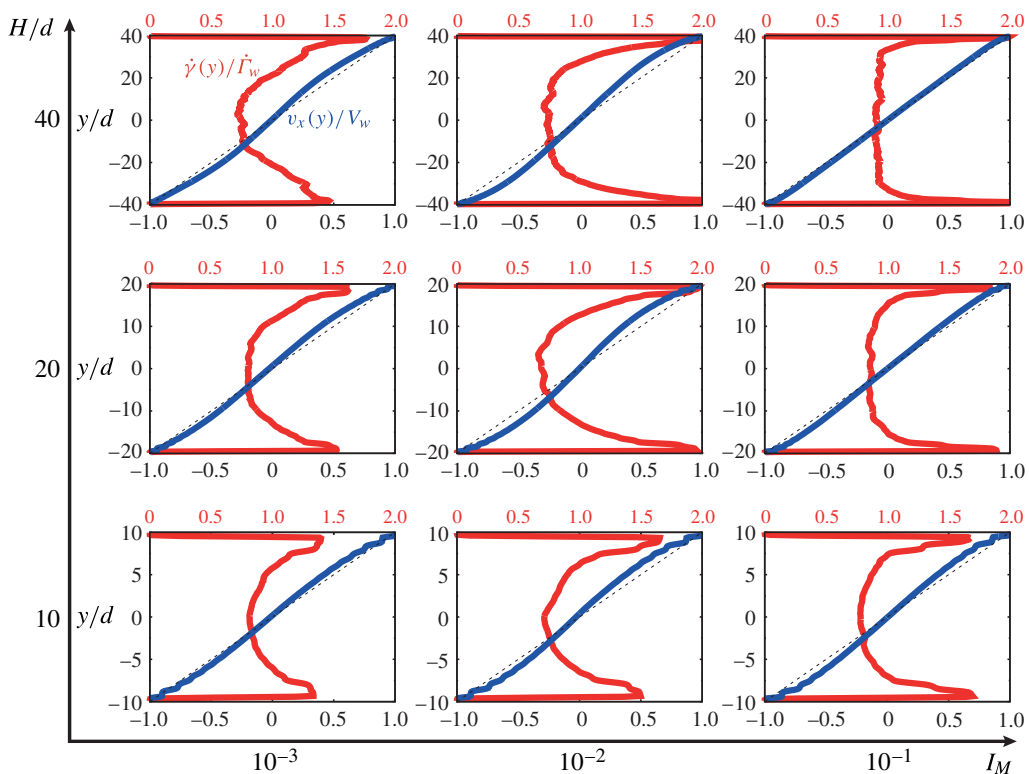
FIGURE 6. (Colour online) Time-averaged velocity and shear rate profiles for flows with various inertial numbers I_M and widths H as indicated by arrows. Same colour code as figure 3(b).
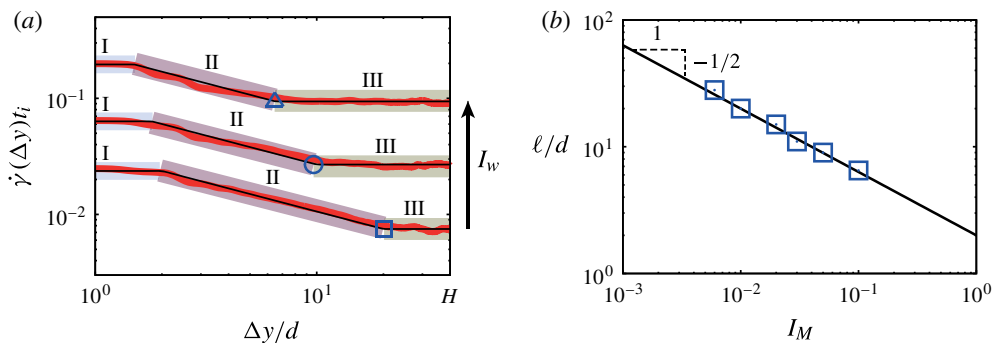

FIGURE 7. (Colour online) (a) Shear rate profiles versus distance to the wall, Δy, for three different inertial numbers, $I_M = 10^{-2}$, 3×10^{-2}, 10^{-1}. Grey curves (red online) represent simulation results and thin black lines the empirical model defined in (4.4). Symbols mark the width, ℓ, of the boundary layer for each system. (b) Width of the boundary layer, ℓ, versus inertial number, I_M; the line represents the function $\ell/d \approx 2 I_M^{-1/2}$.

5.1. *Local constitutive law and viscosity length scale*

The local constitutive laws, as expressed by the friction and dilatancy laws (3.1) and (3.2), fail to capture the wall perturbations as they predict a constant shear rate throughout the layer when the stresses are constant: $\dot{\gamma} = (\mu - \mu_s)/ad\sqrt{\rho/\sigma}$. They nonetheless contain important information regarding the characteristic length scale involved into the diffusion of momentum. This length scale appears when one formulates these laws using the kinetic viscosity ν (m² s⁻¹), which is also referred to as momentum diffusivity, defined as

$$\nu = \frac{1}{\rho}\frac{\partial\dot{\gamma}}{\partial\tau}. \tag{5.1}$$

Using the kinetic viscosity, the friction law becomes

$$\tau = \mu_s\sigma + \rho\nu\dot{\gamma}, \tag{5.2}$$

which is equivalent to a Bingham constitutive law, with a yield stress $\mu_s\sigma$ increasing with the normal stress, and a kinetic viscosity $\nu \propto d\sqrt{P/\rho} = d^2\dot{\gamma}/I$. This kinetic viscosity can be expressed as a function of a typical time scale, $\dot{\gamma}^{-1}$, and a length scale ℓ_ν as

$$\nu \propto \ell_\nu^2\dot{\gamma}, \tag{5.3}$$

$$\ell_\nu \propto \frac{d}{\sqrt{I}}. \tag{5.4}$$

Note that, considering the friction law (3.1), the typical length scale (5.4) can also be expressed as function of the quantity $\mu - \mu_s$: $\ell_\nu \propto d/\sqrt{\mu - \mu_s}$.

Equation (5.4) highlights an important feature of dense granular flows: at low inertial number, the momentum diffuses on a typical length scale much larger than the grain size d. Remarkably, the scaling of this length with I is identical to the scaling of 'cooperativity' length with I, measured and predicted in different configurations within the KEP non-local model framework (Kamrin & Koval 2012; Bouzid *et al.* 2013; Mansard *et al.* 2013).

Quantitative predictions of the viscosity in the zone affected by walls requires identifying the long-range mechanisms underpinning the momentum diffusion. Different analyses have been developed to address this question. Two non-local models, namely the NL process and KEP models, were derived from an analysis of the internal dynamics and the mode of stress propagation within the materials. By contrast, the EV model was developed from the analysis of the internal kinematics and the momentum transport within a non-affine displacement field. Let us now discuss these models and their ability to capture the observed long-range wall perturbations.

5.2. *Non-local self-activated process (NL model)*

This model, introduced in Pouliquen & Forterre (2001, 2009), is based on the following ideas: (i) the shear between two layers of grains leads to topologic rearrangements, also called plastic events, that locally release the stresses; (ii) the associated stress relaxation induces some stress fluctuations that propagate through the network of contact with a typical length scale; (iii) the propagating stress fluctuations contribute to triggering plastic rearrangements far from their origin. In this model, the viscosity at a given point is derived from the sum of the stress fluctuations which have
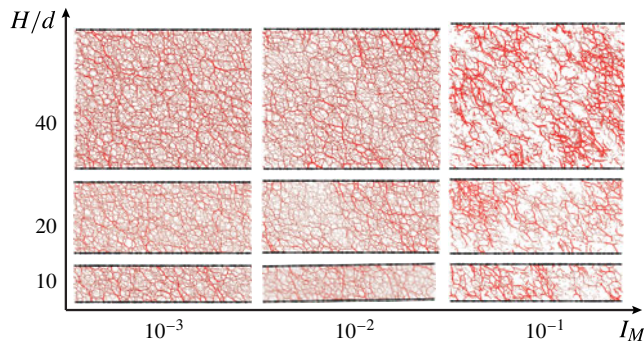
FIGURE 8. (Colour online) Snapshots of the contact network for various inertial numbers, I_w, and system widths H, as indicated by the arrows. The lines connect the centre of each pair of contacting grains. Their thickness is proportional to the normal contact force.

propagated to this point, originating from remote plastic events. As a consequence, the local viscosity depends on the rate of plastic events in the surroundings, and is lower when the shear rate in the surroundings is higher.

Consistent with Hartley & Behringer (2003), Majmudar & Behringer (2005), da Cruz *et al.* (2005), Tordesillas, Zhang & Behringer (2009), Tordesillas *et al.* (2011), Azéma & Radjaï (2014), figure 8 shows that contact force networks within the flows exhibit long length scales, which mechanically connect remote grains to the walls. Further, the contact network seems to be less connected for high values of the inertial number. This supports the relevance of relating non-local behaviour to the force network.

The NL model successfully predicts three observations that the local constitutive law alone is unable to capture: the shear rate profiles within flow in pipes; the dependence of the angle of arrest on the thickness of the granular layer in the inclined plane geometry; more generally, the existence of some flow in zones where the stresses are below the yield stress when there is some flow in the surroundings.

However, the role of the wall is not directly accounted for in the NL model formulation. An additional hypothesis needs to be made regarding the ability of the wall to reflect or absorb stress fluctuations. Considering that the wall absorbs the stress fluctuations, the model predicts that a layer near the wall is subjected to less fluctuation than a layer far from the wall, and its viscosity is higher. Accordingly, the predicted shear rate is lower near the wall, which is not consistent with our results. Assuming that the wall reflects stress fluctuations back into the flow, an opposite trend is predicted that is consistent with our results. Unfortunately, there is no clear rationale to determine whether or not and to what extent walls may reflect stress fluctuations. While the NL model may be able to capture our results, further understanding of the effect of the wall on stress propagation is needed to draw robust conclusions.

5.3. *Non-local KEP model*

This model was introduced in Goyon *et al.* (2008) and Bocquet, Colin & Ajdari (2009) to rationalise the flow of dense emulsions flowing in micro-channels, and was then adapted to dense granular flows in Kamrin & Koval (2012) and Bouzid *et al.* (2013). It is based on the same conceptual ideas as the NL model, considering that

(i) the local viscosity is inversely proportional to the local rate of plastic events; (ii) a plastic event at one location may trigger other plastic events at remote locations through the propagation of stress fluctuations through the contact network.

This model successfully predicts shear rate profiles of soft glassy materials such as emulsions and dry granular matter in geometries where the stresses are not spatially constant, such as pipes, inclined plane and plane shear with gravity, including in zones where the stresses are lower than the yield conditions predicted by their respective local constitutive laws.

In Mansard *et al.* (2013), the non-local KEP model is able to capture wall effects in plane-shear flows of a model dense emulsion. This system has some similarities with the one discussed here: it comprises disks sheared between two rough walls in the absence of gravity, a configuration where stresses are spatially constant. However, it differs from our system in some important points: the disks are soft and interact by strongly dissipative contacts, and the shear was performed at fixed volume and the solid fraction investigated is large, ranging from 90 % to 110 %, which is made possible by large overlaps of soft disks. As a result of these differences, the model emulsion did not satisfy a visco-plastic constitutive law such as (3.1) and (3.2), but instead a Herschel–Bulkley constitutive law typical of soft glassy materials such as foams and emulsions. Nonetheless, in spite of these differences, the reported velocity profiles exhibit an S-shape qualitatively similar to that obtained in our systems. The KEP model, in the plane-shear configuration, can be expressed as

$$\dot{\gamma}(y) - \dot{\gamma}_b = \xi^2 \frac{\partial^2 \dot{\gamma}(y)}{\partial y^2}, \tag{5.5}$$

where ξ is referred to as the 'cooperativity' length, and represents the spatial extent of the non-locality; $\dot{\gamma}(y)$ is the local shear rate, $\dot{\gamma}_b$ the bulk shear rate, which corresponds to the value of the shear rate in a flow with no heterogeneities, e.g. far from the wall in plane-shear flows. To predict the shear rate profile $\dot{\gamma}(y)$, (5.5) can be solved by introducing a boundary condition, the value of the shear rate at the wall, $\dot{\gamma}_w$. The predicted shear rate profile $\dot{\gamma}(y)$ is then

$$\dot{\gamma}(y) = (\dot{\gamma}_w - \dot{\gamma}_b)\frac{\cosh(y/\xi)}{\cosh(H/\xi)} + \dot{\gamma}_b. \tag{5.6}$$

This prediction involves the bulk shear rate, $\dot{\gamma}_b$, the shear rate at the wall, $\dot{\gamma}_w$, and the cooperativity length, ξ. In Mansard *et al.* (2013), this equation was shown to predict S-shape velocity profiles matching the numerical results for a given value of the imposed shear stress and different values of system width H, using a values of $\xi = 2.5d$ and $\dot{\gamma}_w = 1.7\dot{\gamma}_b$.

Figure 9 (*a*i–*a*iii) shows a comparison of the KEP model prediction with our numerical results for three different flows. Equation (5.6) was plotted after measuring $\dot{\gamma}_b$ as the shear rate in the middle of the flow in the largest system, and $\dot{\gamma}_w$ as the maximum value of the shear rate near the walls. Numerical data are well represented using $\xi/d = 5.4$ and $\dot{\gamma}_w/\dot{\gamma}_b = 2.2$ for flow (*a*i), $\xi/d = 5.4$ and $\dot{\gamma}_w/\dot{\gamma}_b = 2.45$ for flow (*a*ii), and $\xi/d = 2.2$ and $\dot{\gamma}_w/\dot{\gamma}_b = 2$ for flow (*a*iii).

A fundamental component of the non-local KEP model is identifying the inverse relation between the viscosity and the rate of plastic rearrangement. This was verified experimentally in Jop *et al.* (2012) and numerically in Mansard *et al.* (2013), by showing that zones of low viscosity exhibit a higher rate of particle rearrangement.
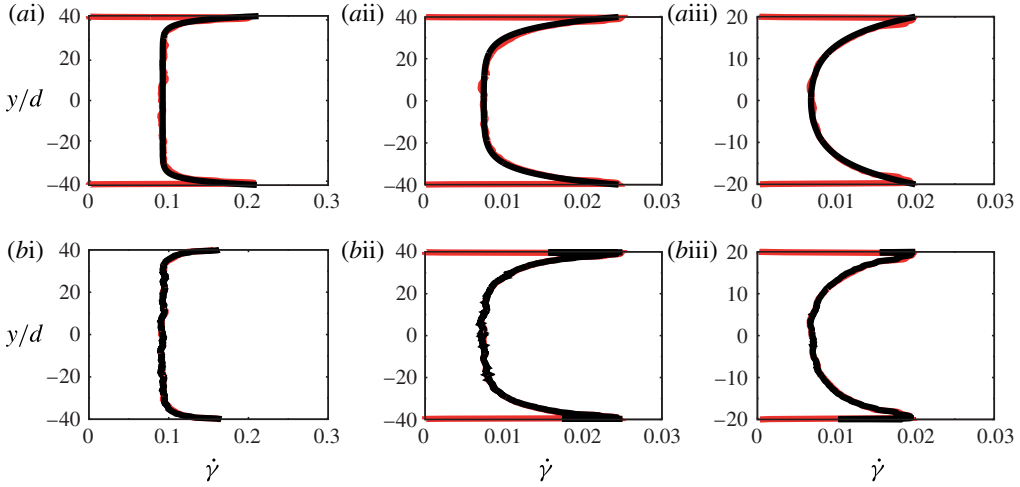
FIGURE 9. (Colour online) Comparison of shear rate profiles between numerical results (grey lines, red online) and and model prediction (black lines). (*a*) The KEP model prediction obtained from (5.6) is shown for three systems: (*a*i) $H/d = 40$, $I_M = 0.1$; (*a*ii) $H/d = 40$, $I_M = 0.01$; and (*a*iii) $H/d = 20$ $I_M = 0.01$. (*b*) The EV model prediction obtained from (5.14) is shown for the same three systems, and with values of β of (*b*i) 3.3, (*b*ii) 2, and (*b*iii) 1.85. Shear rates are expressed in units of inverse of inertial time.

Consistently, it was shown that zones of low viscosity exhibit higher level of velocity fluctuations, thought to be due to the higher rate of rearrangement (Mansard *et al.* 2013).

Figure 10, column (ii), shows the profile of velocity fluctuations δv measured in our systems, defined as the standard deviation of the grain velocity fluctuations $\boldsymbol{v}'_i = \boldsymbol{v}_i - \boldsymbol{v}(y_i)$. Results indicate that the velocity fluctuations are constant in the central region of the flow where the shear rate is constant. Near the walls, where the shear rate is higher and the apparent viscosity lower, the velocity fluctuations do not increase but decrease. This result differs from the measurements reported in Mansard *et al.* (2013), which may be due to the differences in the systems considered. While it does not affect the validity of the KEP model, which relies on the relationship between viscosity and rate of plastic rearrangement, this result suggests that there should exist a mode of grain rearrangement that allows for a higher rate of rearrangement together with lower velocity fluctuations when approaching the walls.

5.4. *Vorticity and vorticity length scale*

Let us now analyse the internal kinematics at the scale of the grains to seek a mechanism consistent with these observations. We focus on the local velocity gradient tensor defined as:

$$\boldsymbol{F}_{\alpha\beta} = \frac{\partial v_\alpha}{\partial x_\beta}, \tag{5.7}$$

which can be measured locally around each grain following a method introduced by Marmottant, Raufaste & Graner (2008) and detailed in appendix B. By definition, the component F_{yx} is equal to the shear rate $\dot{\gamma}$, and the anti-symmetric component of $\boldsymbol{F}_{\alpha\beta}$ is the vorticity w:

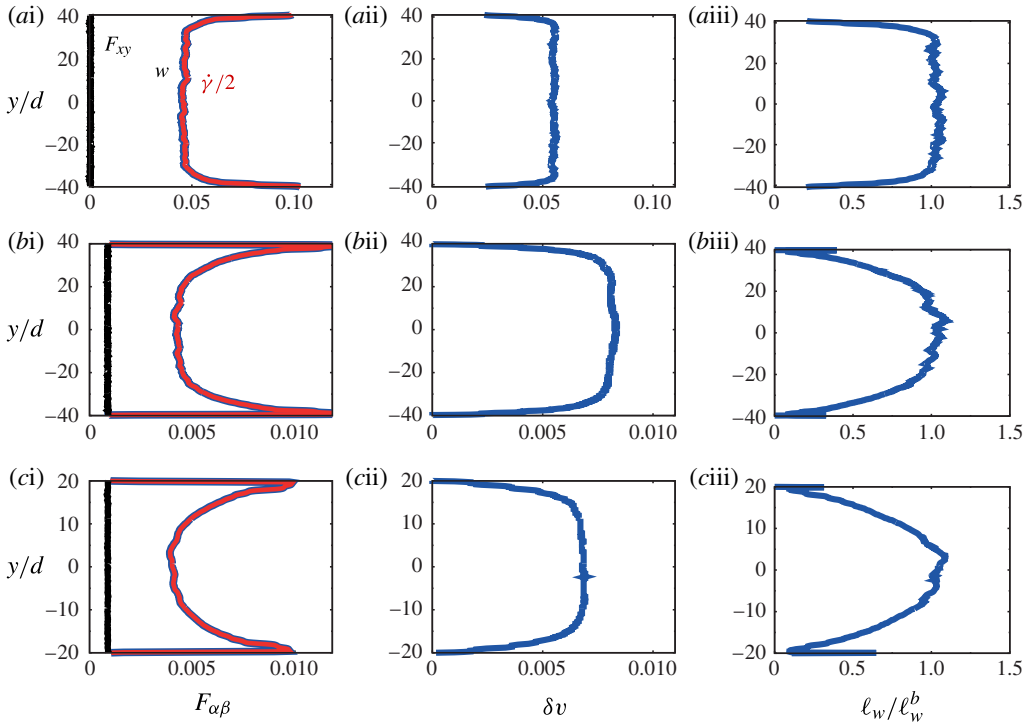$$w = \tfrac{1}{2}(F_{yx} - F_{xy}). \tag{5.8}$$

FIGURE 10. (Colour online) Vorticity and vorticity length scale in three flows: (*a*) $H/d = 40$, $I_M = 0.1$; (*b*) $H/d = 40$, $I_M = 0.01$; (*c*) $H/d = 20$, $I_M = 0.01$. Profiles of shear rate $\dot{\gamma}$, vorticity w and F_{xy} are shown in column (i). Profiles of velocity fluctuations δv are shown in column (ii). Profiles of the deduced vorticity length scale ℓ_w are shown in column (iii), measured according to (5.9) and normalised by the value at the centre of the flow, ℓ_w^b.

Figure 10, column (i), shows the profiles of $F_{xy}(y)$, $\dot{\gamma}(y)$ and $w(y)$ for three different flows ($H/d = 20$ and 40, $I_M = 0.1$ and 0.01). The component F_{xy} appears to always be much smaller than the shear rate $\dot{\gamma}$. As a consequence, there is a direct link between the local shear rate and the vorticity: $w(y) \approx \dot{\gamma}(y)/2$. Accordingly, the vorticity $w(y)$ is higher near the wall and constant in the centre of the flow. This property was consistently observed with all the flows investigated with different width H/d and inertial number I_M.

Figure 11 illustrates snapshots of the local vorticity fluctuation field $w_i' = w_i - \dot{\Gamma}_M/2$. It shows layers of high vorticity near the wall (light grey, red online) and a lower vorticity in the centre of the flow (dark grey, blue online). Further, figure 11 shows that the local vorticity exhibits some spatially correlated patterns comprising large zones with higher or lower vorticity than their surroundings. Note that previous analyses focusing on velocity fluctuations instead of vorticity revealed similar patterns (Blair & Kudrolli 2001; Radjaï & Roux 2002; Mueth 2003; Pouliquen 2004; Brito & Wyart 2007; Behringer *et al.* 2008; Lechenault *et al.* 2008; Liu & Nagel 2010; Abedi & Rechenmacher 2011; Rechenmacher & Abedi 2011; Abedi, Rechenmacher & Orlando 2012; Richefeu, Combe & Viggiani 2012; Miller *et al.* 2013; Miller 2014). Measuring the typical size of these correlated structures is challenging given their seemingly complex shape and large size distribution. As a consequence, statistical
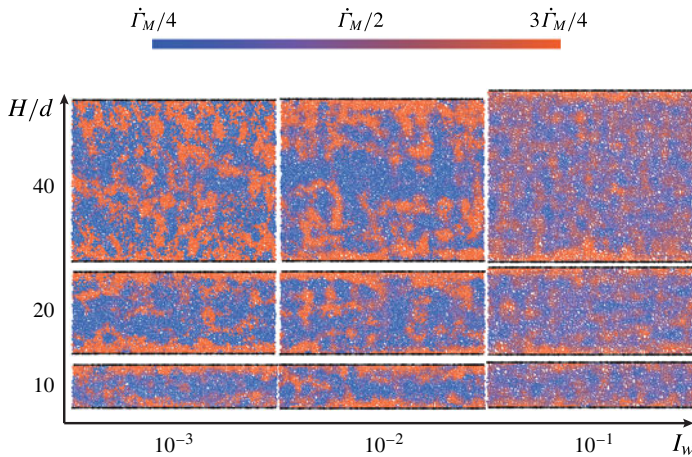
FIGURE 11. (Colour online) Vorticity field snapshots for different system widths, H, and different inertial numbers, I_w, as indicated by the arrows. The local vorticity around each grain is measured according to the method detailed in appendix B.

indicators such as spatial correlations of the vorticity field were found not to be conclusive to measure such a length scale.

Nonetheless, a typical vorticity length scale can be indirectly estimated from the combined measurements of the velocity fluctuation profile and the vorticity profile. The underlying idea is that a vortex of size ℓ_w rotating at a frequency w induces a level of velocity fluctuations of the order of $\delta v \propto w\ell_w$. Thus, the typical length scale associated with the vorticity can be estimated at any location y as

$$\ell_w(y) = \frac{\delta v(y)}{w(y)}. \tag{5.9}$$

Figure 10, column (iii), shows the corresponding profiles of vorticity length scale $\ell_w(y)$. In the bulk of the flow, where the shear rate is constant, the vorticity length is approximately constant: $\ell_w(y) \approx \ell_w^b$. By contrast, close to the walls, the vorticity length scale decreases. Figure 12 shows the values of the bulk vorticity length ℓ_w^b measured in the largest system ($H/d = 40$) as a function of the macroscopic inertial number I_M. It follows a power law:

$$\ell_w^b \propto \frac{d}{I_M^{1/2}}, \tag{5.10}$$

which is remarkably similar to the wall perturbation range empirically determined in (4.5), to the length scale of granular momentum diffusivity deduced from the local friction law in (5.3), and to the cooperativity length scale measured and predicted in the KEP framework (Kamrin & Koval 2012; Bouzid *et al.* 2013; Mansard *et al.* 2013).

To summarise, we extracted a vorticity length scale from the measurements of the velocity fluctuations. When approaching the walls, where the shear rate of the material increases, this length scale is found to decrease. This trend can be understood since, close to the walls, the lack of space mean that the correlated structures cannot freely develop: the presence of the wall tends to truncate the largest possible vortex in the flow. Let us now present a non-local model based on vorticity that could quantitatively capture the wall perturbations.
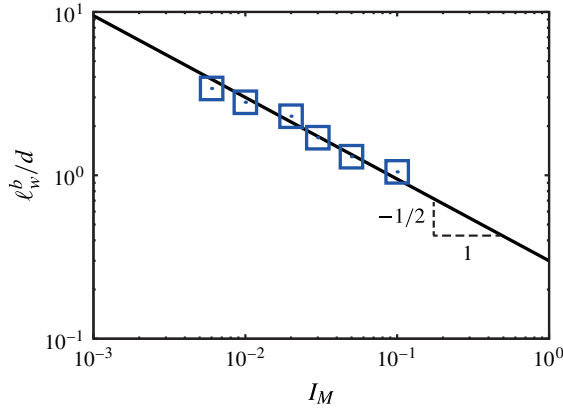
FIGURE 12. (Colour online) Vorticity length scale in the bulk of the flow, ℓ_w^b, as a function of the macroscopic inertial number, I_M, measured in the largest systems, $H/d = 40$. The line represents the power law in (5.10).

5.5. *EV model*

The EV model was first developed in the context of turbulent flows of Newtonian fluids to explain the increase in apparent viscosity observed between turbulent and laminar flow regimes. The underlying ideas are (i) there is an intrinsic viscosity ν_0 due to the transfer of momentum by molecular collisions in both regimes and (ii) in turbulent regimes, vortices develop and lead to an additional mode of momentum transfer and an associated viscosity ν^{eddy}. The effective viscosity ν^{eff} is thus expressed as the sum of the two contributions:

$$\nu^{eff} = \nu_0 + \nu^{eddy}. \tag{5.11}$$

Prandtl's mixing length model provides an estimation of the typical momentum diffusivity associated with a vortex of size ℓ_w rotating at a frequency w, as

$$\nu^{eddy} \propto w\ell_w^2. \tag{5.12}$$

In Staron *et al.* (2010) and Miller *et al.* (2013), the EV model was adapted to dense granular flows in the inclined-plane and plane-shear geometries. Both approaches consist of considering two mechanisms of momentum transfer in granular materials: pairwise grain collisions and large-scale vortex rotations. Accordingly, the apparent granular viscosity (5.3) can be expressed by

$$\nu = d^2\dot{\gamma} + \beta\ell_w^2\dot{\gamma}, \tag{5.13}$$

where β denotes a numerical constant reflecting the actual contribution to momentum transfer of vortices. The first term represents the diffusion of momentum by grain collision and the second term that by rotation of vortices of size ℓ_w. Note that the corresponding effective length scale of momentum diffusion would then be $\ell_\nu = d\sqrt{1 + \beta(\ell_w/d)^2}$. Introducing this expression for viscosity into the friction law (3.1) leads to the following prediction of the shear rate profile:

$$\dot{\gamma}(y) = \frac{A}{\sqrt{1 + \beta\,(\ell_w(y)/d)^2}}, \tag{5.14}$$

with $A = (\mu - \mu_s/a)(1/d\sqrt{\rho/\sigma})$.

In Staron *et al.* (2010) and Miller *et al.* (2013), no vorticity length scale was measured or estimated. This length scale was assumed to be given by some function of the distance to the walls. Various functions of the distance to the wall were introduced, so that the model (5.13) would predict the correct viscosity variation near walls. However, there is no established rationale for the choice of this function, and different choices may equally well represent the results.

In our systems, a typical vorticity length scale ℓ_w was estimated from the analysis of the grain velocity fluctuations, and can thus directly be introduced in (5.14). Figure 9 (*b*i–*b*iii) shows that the prediction of this model can successfully match the numerical results. The parameter A was directly measured as the shear rate at the wall, $\dot{\gamma}(y = H)$, using the fact that the vortex size $\ell_w(H)$ tends to zero, as shown on figure 10; β is thus the only fitting parameter, with values of the order of 2.

The empirical model (4.4) for wall perturbations can be interpreted within the EV framework. Zone III corresponds to the region in the middle of the flow where the vorticity length scale can fully develop: it is not affected by the walls. Zone II corresponds to the region where the vorticity length scale is truncated by the proximity of the walls, yet it still contributes significantly to the effective viscosity. Zone I corresponds to the first layers of grains near the wall where the vorticity length scale is so small that the grain collisions become the dominant mode of momentum transfer. Given that the EV model, (5.14), correctly captures the shear rate profiles, i.e. $\dot{\gamma} \propto \Delta y^{-1/2}$ in zone II, the vorticity length must scale as $\ell_w(y)/d \propto (\Delta y/d)^{1/2}$ when approaching the walls and not as $\ell_w(y) \propto \Delta y$ as is usually assumed in EV models.

6. Conclusion

The discrete element method simulations of plane-shear flow between walls presented in this paper show that walls significantly affect the viscosity of dense granular flows over large distances. Near walls, the viscosity is much lower than in the bulk flow. The range of this perturbation can reach several dozens of grains and increases for slower flows.

The practical implication of these results is to question a common way to measure the constitutive law of granular materials. Often, both experimentally and numerically, these laws are measured by averaging stresses or strain rate over the entire system width. We observed on figure 2 that both the friction law and the dilatancy laws measured by this method exhibit strong and non-trivial system size dependences, which results from a combination of the material constitutive behaviour and wall effects. We compare two different non-local models, namely the KEP and the EV models, which are able to rationalise these wall effects.

Interestingly, the KEP and EV models arise from radically different analyses of the mechanisms underpinning non-local effects. On one hand, the KEP model is developed by considering the non-local dynamic of the system, namely the stress propagation through the contact network. On the other hand, the EV model is developed by considering the non-local kinematics of the system, namely the existence of structures of grains rotating in a correlated fashion and their contribution to the momentum transfer. The fact that both models are able to capture the long-range wall perturbations suggests that force networks and vorticity may be intimately related in granular flows. Establishing such a connection constitutes a promising research avenue to further understand non-local behaviours.

The strength of the KEP model is its ability to capture many non-trivial behaviours of dense granular flows in geometries with a stress gradient. However, it is

comparatively weaker in predicting wall perturbations, given that it then critically relies on a parameter, the fluidity at the wall. To date, there is no prediction of this parameter, which must be determined empirically. Then, the KEP correctly captures the shear increase measured close to the walls. This increase is associated with a decrease of the viscosity which, in the KEP framework, arises from an increase of the number of rearrangements. One could expect that a local increase of the shear rate and of the number of rearrangements should lead to an increase of the velocity fluctuations. However, we observe the opposite trend in our simulation results.

The EV model involves the length scale associated with the vorticity. When approaching the walls, due to the lack of space, the largest possible vortex becomes smaller and smaller. This trend was shown by measuring the vorticity length scale from the local velocity fluctuations and the local vorticity, see (5.9). Using the EV model, we can introduce this length scale in the local constitutive friction law. This predicts the correct shear rate profiles and is also consistent with the decrease of the velocity fluctuations observed near the walls.

This study suggests that the vorticity length scale can be a key parameter to further understand the non-local behaviour of grains within dense granular flows. This length scale was found to exhibits a striking correlation with the material viscosity, and to significantly vary in the large zone affected by the walls. The EV model provides the rationale between the material viscosity and its vorticity length scale. Finding a link between the cooperativity length scale of the KEP and this vorticity length scale is a promising question.

Similarly, the vorticity analysis developed here for dry granular flows could help further understand non-local effects in other particulate fluids such as such as suspensions (Bonnoit *et al.* 2010*a*,*b*; Nordstrom, Gollub & Durian 2011), flowing blood cells (Freund 2014), foams (Sexton, Möbius & Hutzler 2011; Hagans & Feitosa 2013) and emulsions (Goyon *et al.* 2008).

Acknowledgements

Appendix A. Discrete element simulation

Dense granular flows are simulated using discrete element method, such as introduced by Cundall & Strack (1979). The motion of each grain, both translation and rotation, is integrated over small time steps dt using a second-order predictor–corrector scheme. The acceleration and angular acceleration of each grain is evaluated at each time step as a function of the force and momentum balance, including contact forces between pairs of grains. The contact forces involve a normal elastic repulsion F^{ela}. A small overlap between two grains i and j is possible, $\delta_{ij}^n = \|X_j - X_i\| - (R_i + R_j)$, with X denoting the position of the grain centre and R its radius.

The elastic force that grain i experiences is then proportional to that overlap, $\boldsymbol{F}_{ij}^{ela} = ER_{ij}\delta_{ij}^n\boldsymbol{n}_{ij}$, where $\boldsymbol{n}_{ij} = (X_j - X_i)/(\|X_j - X_i\|)$ is the unit vector normal to the surface of grain i at the contact point, $R_{ij} = (R_iR_j)/(R_i + R_j)$ is the effective radius of the contact and E is an elastic constant of the order of Young's modulus of the grains. Note that the linear Hookean elastic model chosen here is consistent with the elastic contact between two two-dimensional disks (or two cylinders). Hertzian nonlinear elasticity would represent the elastic force between two spheres. The force would then

be $\boldsymbol{F}_{ij}^{ela} = ER_{ij}^2(\delta_{ij}^n/R_{i}j)^{3/2}\boldsymbol{n}_{ij}$. We consider here rather stiff grains, with small elastic deformations. The typical overlap δ^n is of the order of $\kappa = \sigma_w/E = 10^{-3}$. Then, both the Hertzian and Hookean models are equivalent at the first order.

Normal collisions between two grains dissipate energy. This is represented by a viscous-like normal force $\boldsymbol{F}_{ij}^{vis}$, proportional to the grains relative normal velocity, $\boldsymbol{F}_{ij}^{vis} = -\zeta\|\boldsymbol{V}_j - \boldsymbol{V}_i\|\boldsymbol{n}_{ij}$. The coefficient ζ is related to Newton's coefficient of restitution e, the ratio of post- to pre-impact relative velocities in a binary collision: $\zeta = \sqrt{m_{ij}ER_{ij}}(-2\log(e)/\sqrt{\pi^2 + \log(e)^2})$, with $m_{ij} = (m_i * m_j)/(m_i + m_j)$ the effective mass of the two colliding grains.

Grains are frictional, and a friction force $\boldsymbol{F}^{fri}$ is introduced, tangential to the contact. Grains may deform elastically in the tangent direction. The tangential force evolution, $\dot{F}^{fri}$ is driven by the tangential deformation evolution, $\dot{F}^{fri} = \Delta V_{ij}^t dt\, ER_{ij}$, with ΔV_{ij}^t denoting the relative velocity at the contact point, including grain translation and rotation. This tangential elastic force is limited by a Coulomb criterion involving the grain-to-grain coefficient of friction μ_g. If $\|F^{fri}\| = \mu_g\|F^{ela}\|$, the grains slide and $\|\dot{F}^{fri}\|$ can only decrease. Rolling resistance and twist torque, which could be introduced as in Rognon, Einav & Gay (2010), are not included here. The friction forces are then the only component of the contact interaction that induces torque and grain rotation.

Appendix B. Averaging method

In this paper, various quantities are presented in the form of a profile in the y direction, averaged in time. The method of averaging consists of considering a series of snapshots, typically 100. For each snapshot, the system is divided into slices of size $d/10$. The properties of each grain, such as its velocity, are collected in each slice and weighted by the surface of the grains that belong to the slice, w_i^s. The average velocity in a slice at the position y_s is thus $\boldsymbol{v}(y_s) = \sum_i \boldsymbol{V}_i w_i^s / \sum_i w_i^s$, where the sum runs over all the grains. The solid fraction in that slice is $\langle\phi(y_s)\rangle = \sum_i w_i^s/(0.1dL)$. The final time-averaged profile is obtained by averaging all these instantaneous profiles.

The time-averaged velocity gradient profile, $\dot{\gamma}(y_s)$, can be deduced by differentiating the velocity profile obtained with the method just described. However, this differentiation induces a large level of noise. We preferred to evaluate, for each grain at each time step, the local velocity gradient tensor $\boldsymbol{F}_{\alpha\beta}$ following the method introduced in Marmottant *et al.* (2008):

$$\boldsymbol{F}_{\alpha\beta} = \langle\boldsymbol{l}_{ij}\otimes\boldsymbol{l}_{ij}\rangle^{-1}\cdot\langle\boldsymbol{l}_{ij}\otimes\boldsymbol{V}_{ij}\rangle. \tag{B 1}$$

The symbols $\cdot$ and $\otimes$ denote the tensor product and the outer product, respectively. The symbol $\langle\cdot\rangle$ represents the average of pairs of neighbouring grains i and j, with a centre-to-centre vector $\boldsymbol{l}_{ij}$ and a relative translation velocity $\boldsymbol{V}_{ij} = \boldsymbol{V}_j - \boldsymbol{V}_i$ (see figure 13). Note that these neighbouring grains may or may not be contacting. A cutoff distance of $1.5d$ was chosen to ensure that the averaging is performed on a zone as small as possible, with enough neighbours to evaluate the velocity gradient. Different values of cutoff were tested with no significant change in the results. The velocity gradient profile $\dot{\gamma}(y_s)$ is then obtained by averaging the relevant component of the tensor $\boldsymbol{F}$ with the slice method described above.
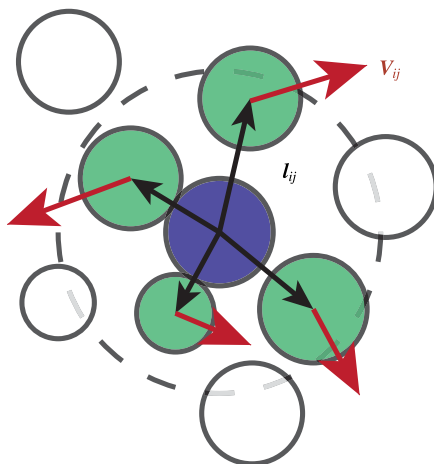
FIGURE 13. (Colour online) Local velocity gradient measurement. The local velocity gradient tensor can be estimated for each grain by considering the neighbouring grains, their relative position and relative velocity according to (B 1). Here, the velocity gradient associated with the dark central grain (purple online) involves the lighter grains (green online), but excludes the white grains, which are further away than the cutoff distance represented by the dashed circle.

REFERENCES

ABEDI, S. & RECHENMACHER, A. 2011 Vortex structures inside shear bands in sands. In *Multiscale and Multiphysics Processes in Geomechanics*, pp. 21–24. Springer.

ABEDI, S., RECHENMACHER, A. L. & ORLANDO, A. D. 2012 Vortex formation and dissolution in sheared sands. *Granul. Matt.* **14** (6), 695–705.

ANDREOTTI, B. 2007 A mean-field model for the rheology and the dynamical phase transitions in the flow of granular matter. *Europhys. Lett.* **79** (3), 34001.

ANDREOTTI, B., FORTERRE, Y. & POULIQUEN, O. 2013 *Granular Media: Between Fluid and Solid*. Cambridge University Press.

AZÉMA, E. & RADJAÏ, F. 2014 Internal structure of inertial granular flows. *Phys. Rev. Lett.* **112** (7), 078001.

BEHRINGER, R. P., DANIELS, K. E., MAJMUDAR, T. S. & SPERL, M. 2008 Fluctuations, correlations and transitions in granular materials: statistical mechanics for a non-conventional system. *Phil. Trans. R. Soc. Lond.* A **366** (1865), 493–504.

BLAIR, D. L. & KUDROLLI, A. 2001 Velocity correlations in dense granular gases. *Phys. Rev.* E **64** (5), 050301.

BOCQUET, L., COLIN, A. & AJDARI, A. 2009 Kinetic theory of plastic flow in soft glassy materials. *Phys. Rev. Lett.* **103** (3), 36001.

BONNOIT, C., DARNIGE, T., CLEMENT, E. & LINDNER, A. 2010a Inclined plane rheometry of a dense granular suspension. *J. Rheol.* **54**, 65–79.

BONNOIT, C., LANUZA, J., LINDNER, A. & CLEMENT, E. 2010b Mesoscopic length scale controls the rheology of dense suspensions. *Phys. Rev. Lett.* **105** (10), 108302.

BOUZID, M., TRULSSON, M., CLAUDIN, P., CLÉMENT, E. & ANDREOTTI, B. 2013 Nonlocal rheology of granular flows across yield conditions. *Phys. Rev. Lett.* **111** (23), 238301.

BRITO, C. & WYART, M. 2007 Heterogeneous dynamics, marginal stability and soft modes in hard sphere glasses. *J. Stat. Mech.* **2007** (8), L08003.

DA CRUZ, F., CHEVOIR, F., ROUX, J. N. & IORDANOFF, I. 2004 Macroscopic friction of dry granular materials. In *Transient Processes in Tribology* (ed. G. Dalmaz, A. A. Lubrecht, D. Dowson & M. Priest), pp. 53–61. Elsevier.

DA CRUZ, F., EMAM, S., PROCHNOW, M., ROUX, J.-N. & CHEVOIR, F. 2005 Rheophysics of dense granular materials: discrete simulation of plane shear flows. *Phys. Rev.* E **72**, 021309.

CUNDALL, P. A. & STRACK, O. D. L. 1979 A discrete numerical model for granular assemblies. *Géotech.* **29**, 47–65.

FORTERRE, Y. & POULIQUEN, O. 2008 Flows of dense granular media. *Annu. Rev. Fluid Mech.* **40**, 1–24.

FREUND, J. B. 2014 Numerical simulation of flowing blood cells. *Annu. Rev. Fluid Mech.* **46**, 67–95.

GDR MIDI 2004 On dense granular flows. *Eur. Phys. J.* E **14**, 341–365.

GOUJON, C., THOMAS, N. & DALLOZ-DUBRUJEAUD, B. 2003 Monodisperse dry grain flows on inclined planes: role of roughness. *Eur. Phys. J.* E **11**, 147–157.

GOYON, J., COLIN, A., OVARLEZ, G., AJDARI, A. & BOCQUET, L. 2008 Spatial cooperativity in soft glassy flows. *Nature* **454** (7200), 84–87.

HAGANS, N. & FEITOSA, K. 2013 Extensional rheology of a two dimensional foam. *Bull. Am. Phys. Soc.* **58**, 1198.

HARTLEY, R. R. & BEHRINGER, R. P. 2003 Logarithmic rate dependence of force networks in sheared granular materials. *Nature* **421** (6926), 928–931.

JOP, P., FORTERRE, Y. & POULIQUEN, O. 2006 A constitutive law for dense granular flows. *Nature* **441**, 727–730.

JOP, P., MANSARD, V., CHAUDHURI, P., BOCQUET, L. & COLIN, A. 2012 Microscale rheology of a soft glassy material close to yielding. *Phys. Rev. Lett.* **108**, 148301.

KAMRIN, K. & KOVAL, G. 2012 Nonlocal constitutive relation for steady granular flow. *Phys. Rev. Lett.* **108** (17), 178301.

LECHENAULT, F., DAUCHOT, O., BIROLI, G. & BOUCHAUD, J.-P. 2008 Critical scaling and heterogeneous superdiffusion across the jamming/rigidity transition of a granular glass. *Europhys. Lett.* **83** (4), 46003.

LIU, A. J. & NAGEL, S. R. 2010 The jamming transition and the marginally jammed solid. *Annu. Rev. Condens. Matter Phys.* **1** (1), 347–369.

MAJMUDAR, T. S. & BEHRINGER, R. P. 2005 Contact force measurements and stress-induced anisotropy in granular materials. *Nature* **435** (7045), 1079–1082.

MANSARD, V., COLIN, A., CHAUDHURI, P. & BOCQUET, L. 2013 A molecular dynamics study of non-local effects in the flow of soft jammed particles. *Soft Matt.* **9** (31), 7489–7500.

MARMOTTANT, P., RAUFASTE, C. & GRANER, F. 2008 Discrete rearranging disordered patterns, part II: 2D plasticity, elasticity and flow of a foam. *Phys. Rev.* E **25** (4), 371–384.

MILLER, T. 2014, The kinematics of dense granular materials under indefinite plane-shear. PhD thesis, School of Civil Engineering, The University of Sydney.

MILLER, T., ROGNON, P., METZGER, B. & EINAV, I. 2013 Eddy viscosity in dense granular flows. *Phys. Rev. Lett.* **111** (5), 058002.

MOHAN, L. S., RAO, K. K. & NOTT, P. R. 2002 Frictional Cosserat model for slow shearing of granular materials. *J. Fluid Mech.* **457**, 377–409.

MUETH, D. M. 2003 Measurements of particle dynamics in slow, dense granular couette flow. *Phys. Rev.* E **67** (1), 011304.

NORDSTROM, K. N., GOLLUB, J. P. & DURIAN, D. J. 2011 Dynamical heterogeneity in soft-particle suspensions under shear. *Phys. Rev.* E **84** (2), 021403.

POULIQUEN, O. 2004 Velocity correlation in dense granular flows. *Phys. Rev. Lett.* **93**, 248001.

POULIQUEN, O. & FORTERRE, Y. 2001 Slow dense granular flows as a self-induced process. *Adv. Complex Syst.* **4**, 441–450.

POULIQUEN, O. & FORTERRE, Y. 2009 A non-local rheology for dense granular flows. *Phil. Trans. R. Soc. Lond.* A **367** (1909), 5091–5107.

RADJAÏ, F. & ROUX, S. 2002 Turbulentlike fluctuations in quasistatic flow of granular media. *Phys. Rev. Lett.* **89** (6), 064302.

RECHENMACHER, A. L. & ABEDI, S. 2011 Length scales for nonaffine deformation in localized, granular shear. In *Advances in Bifurcation and Degradation in Geomaterials*, pp. 59–65. Springer.

RICHEFEU, V., COMBE, G. & VIGGIANI, G. 2012 An experimental assessment of displacement fluctuations in a 2d granular material subjected to shear. *Géotech. Lett.* **2** (July–September), 113–118.

ROGNON, P., EINAV, I. & GAY, C. 2010 Internal relaxation time in immersed particulate materials. *Phys. Rev.* E **81**, 061304.

ROGNON, P. G., ROUX, J. N., NAAÏM, M. & CHEVOIR, F. 2007 Dense flows of bidisperse assemblies of disks down an inclined plane. *Phys. Fluids* **19**, 058101.

ROGNON, P. G., ROUX, J. N., NAAIM, M. & CHEVOIR, F. 2008 Dense flows of cohesive granular materials. *J. Fluid Mech.* **596**, 21–47.

ROGNON, P. G., ROUX, J.-N., WOLF, D., NAAIM, M. & CHEVOIR, F. 2006 Rheophysics of cohesive granular materials. *Europhys. Lett.* **74**, 644–650.

SEXTON, M. B., MÖBIUS, M. E. & HUTZLER, S. 2011 Bubble dynamics and rheology in sheared two-dimensional foams. *Soft Matt.* **7** (23), 11252–11258.

SHOJAAEE, Z., BRENDEL, L., TÖRÖK, J. & WOLF, D. E. 2012a Shear flow of dense granular materials near smooth walls. II. Block formation and suppression of slip by rolling friction. *Phys. Rev.* E **86** (1), 011302.

SHOJAAEE, Z., ROUX, J. N., CHEVOIR, F. & WOLF, D. E. 2012b Shear flow of dense granular materials near smooth walls. I. Shear localization and constitutive laws in the boundary region. *Phys. Rev.* E **86** (1), 011301.

STARON, L. 2008 Correlated motion in the bulk of dense granular flows. *Phys. Rev.* E **77** (5), 051304.

STARON, L., LAGRÉE, P.-Y., JOSSERAND, C. & LHUILLIER, D. 2010 Flow and jamming of a two-dimensional granular bed: toward a nonlocal rheology? *Phys. Fluids* **22**, 113303.

TORDESILLAS, A., LIN, Q., ZHANG, J., BEHRINGER, R. P. & SHI, J. 2011 Structural stability and jamming of self-organized cluster conformations in dense granular materials. *J. Mech. Phys. Solids* **59** (2), 265–296.

TORDESILLAS, A., ZHANG, J. & BEHRINGER, R. 2009 Buckling force chains in dense granular assemblies: physical and numerical experiments. *Geomech. Geoengin.* **4** (1), 3–16.